Conical nanopores highlight the pro-aggregating effects of pyrimethanil fungicide on Aβ(1–42) peptides and dimeric splitting phenomena

Nathan Meyer, Nicolas Arroyo, Matteo Baldelli, Nicolas Coquart, Jean-Marc Janot, Véronique Perrier, Mauro Chinappi, Fabien Picaud, Joan Torrent, Sebastien Balme

Conical nanopores highlight the pro-aggregating effects of pyrimethanil fungicide on Aβ(1-42) peptides and dimeric splitting phenomena

*Nathan Meyer[a]†, Nicolas Arroyo[b]†, Matteo Baldelli[c]†, Nicolas Coquart[a], Jean Marc Janot[a], Veronique Perrier[d], Mauro Chinappi[c], Fabien Picaud[b], Joan Torrent[d], Sebastien Balme[a]**

[a]Institut Européen des Membranes, UMR5635 UM ENCSM CNRS, Place Eugène Bataillon, 34095 Montpellier cedex 5, France.

[b]Laboratoire de Nanomédecine, Imagerie et Thérapeutique, EA4662, Université Bourgogne-Franche-Comté (UFR Sciences et Techniques), Centre Hospitalier Universitaire de Besançon, 16 route de Gray, 25030 Besançon, France

[c]Dipartimento di Ingegneria Industriale, Università di Roma Tor Vergata, Via del Politecnico 1, 00133 Roma, Italia

[d] INM, University of Montpellier , INSERM, Montpellier, France

† equal contribution,

*corresponding authors. Sebastien.balme@umontpellier.fr

Abstract

The Aβ(1-42) aggregation is a key event in the physiopathology of Alzheimer's disease (AD). Exogenous factors such as environmental pollutants, and more particularly pesticides, can corrupt Aβ(1-42) assembly and could influence the occurrence and pathophysiology of AD. However, pesticide involvement in the early stages of Aβ(1-42) aggregation is still unknown. Here, we employed conical track-etched nanopore in order to analyse the Aβ(1-42) fibril formation in the presence of pyrimethanil, a widely used fungicide belonging to the anilinopyrimidine class. Our results evidenced a pro-aggregating effect of pyrimethanil on Aβ(1-42). Aβ(1-42) assemblies were successfully detected using conical nanopore coated with PEG. Using an analytical model, the large current blockades observed (>0.7) were assigned to species with size close to the sensing pore. The long dwell times (hundreds ms scale) were interpreted by the possible interactions amyloid/PEG using molecular dynamic simulation. Such interaction could leave until splitting phenomena of the dimer structure. Our work also evidences that the pyrimethanil induce an aggregation of Aβ(1-42) mechanism in two steps including the reorganization prior the elongation phase.

Keywords: amyloid, nanopore, resistive pulse, fungicide, Aβ(1-42), track-etched, lag phase,

1. Introduction

The assembly of normally soluble proteins into an amyloid fold has become the dominant model that explains the pathogenesis of numerous neurodegenerative disorders, including Alzheimer's (AD) and Parkinson's diseases (Chiti and Dobson, 2017; Ke et al., 2020). This critical misfolding pathway, called amyloidogenesis, is guiding the development of potential treatments since it generates structurally different protein assemblies that are thought to be responsible for the cellular toxicity (Soto and Pritzkow, 2018). Although unexpectedly diverse and complex, the amyloid fold is structurally characterized by a typical cross-β fibril architecture and is often considered to be energetically the most favourable protein state (Gazit,

2002). Nevertheless, amyloids are dynamic, with monomers/oligomers association and dissociation from their ends and surface (Carulla et al., 2010; Jahn and Radford, 2008). In vitro, kinetic growth curves for Aβ(1-42) fibril formation starting from pure monomer display a sigmoidal profile, where after a first slow amyloid size increase (lag phase), the aggregates start to growth (growth phase) until saturation is reached. Oligomeric species populated during the lag phase are heterogeneous and rapidly evolve to amyloid fibrils during the growth phase, in which fibril mass increases with time to an equilibrium plateau (Michaels et al., 2018). There is compelling evidence that different physicochemical factors can influence the duration of the lag phase. The search for a trigger event leading to an accelerated Aβ(1-42) fibril formation has mostly been investigated from the perspectives of the properties of Aβ itself (i.e., mutations, truncations), but marginally from abnormal interactions with exogenous synthetic molecules (McLaurin et al., 2000).

Indeed, environmental pollutants are now suspected to play a role in the aetiology or incidence of neurological disorders (Chin-Chan et al., 2015). Epidemiological studies revealed that occupational exposure of farmers to organophosphates has been associated with an increased risk to develop Alzheimer's disease (Hayden et al., 2010). Three fungicides belonging to the anilinopyrimidine class, i.e. cyprodinil, mepanipyrim and pyrimethanil are widely used for crop preservation, as well as for long-term storage of fruits and vegetables. Many reports have in the past established their presence in our environment, food as well as in baby food jars(Nougadère et al., 2020; Sánchez-Santed et al., 2016) . Recently, enhanced Aβ aggregation, microgliosis and neuronal loss have been observed after treatment of AD transgenic mouse model with residual amounts (0.1 µg/L in drinking water for 9 months) of a cocktail of 3 fungicides, cyprodinil, mepanipyrim, and pyrimethanil (Lafon et al., 2020). Aβ pro-aggregating activity appears to be mediated by the direct interaction of fungicides with Aβ(1-42). Nevertheless, the influence of such chemical agents in Aβ(1-42) assembly, and

amyloidogenesis, as well as their interplay with specific subsets of Aβ(1-42) assemblies remain to be determined.

While the underlying molecular events occurring during Aβ(1-42) fibril growth are now widely recognized, less is known about the transient oligomers formed at earlier stages especially during the lag phase. The reason is that conventional techniques do not provide sufficient resolution to detect and characterize these intermediate species in bulk assays. Therefore, an experimental technique is needed allowing for high-sensitive real-time detection and characterization of early stages of Aβ(1-42) assembly. Recently, the use of nanopore technology demonstrated very promising results thanks to the possibility to obtain information about the protein aggregate population under continuous measurement(Houghtaling et al., 2018b). Biological nanopores were widely used for protein sensing. They were shown to be able to detect minor differences in peptide sequences (Asandei et al., 2017; Huang et al., 2019; Ouldali et al., 2020; Piguet et al.) and to analyse the protein folding/unfolding process (Di Marino et al., 2015; Merstorf et al., 2012; Oukhaled et al., 2007; Rodriguez-Larrea and Bayley, 2013). They were used to investigate the prion protein and α-synuclein misfolding (Madampage et al., 2012; Stefureac et al., 2008; Tavassoly and Lee, 2012), Aβ peptide aggregation (Bonome et al., 2019; Wang et al., 2011) or binding with metal ion (Asandei et al., 2013; Asandei et al., 2014). The Aβ(1-42) aggregation was evidenced by α-hemolysin as bumping event, making it impossible to obtain information about the amyloid size (Wang et al., 2011). The solid-state nanopores have advantages of robustness, reusability and scalable diameter (Lepoitevin et al., 2017). They allow the characterization of conformational fluctuations of proteins (Waduge et al., 2017), their interactions with nanoparticles (Coglitore et al., 2018; Coglitore et al., 2019) as well as protein aggregation. The unmodified SiN nanopore allows detection of lysozyme oligomers (Balme et al., 2016). The glass nanopipettes are also used for amyloid detection as shown for lysozyme (Martyushenko et al., 2015), α-synuclein (Chau et al., 2020) and Aβ(1-42)

(Yu et al., 2019). However, the nanopore functionalization is required to prevent the nanopore fouling in the case of Aβ(1-40) (Yusko et al., 2011) or α-synuclein (Hu et al.), and to allow discrimination of oligomers (Yusko et al., 2012). The functionalization with PEG is efficient to discriminate different types of protein aggregates (Giamblanco et al., 2018b) while at the same time increasing the nanopore lifetime (Roman et al., 2017). The limitation of solid-state nanopores and glass nanopipettes is that they do not allow to differentiate aggregates and protofibrils larger than the nanopore diameter. Indeed, when the aggregates are larger than the pore, only bumping events are observed making the size discrimination impossible. To overcome this problem, our group proposed the use of conical track-etched nanopore (Giamblanco et al., 2018a). The latter are more used for their ionic-diode properties than single molecule sensing (Ma et al., 2020; Zhao et al., 2017). However, by combining this geometry and a very long lifetime, they are more convenient to monitor protein aggregation kinetic (Giamblanco et al., 2018a; Giamblanco et al., 2020a) as well as their enzymatic degradation (Giamblanco et al., 2020b).

To investigate the influence of extrinsic factors on Aβ(1-42) assembly we selected the fungicide pyrimethanil, which belongs to the anilinopyrimidine class. In this work, the Aβ(1-42) amyloidogenesis in the absence and presence of pyrimethanil was monitored by a thioflavin T (ThT) binding assay, and characterized using conical track-etched nanopore technology as an *ex-situ* assay. Using this up-to-date approach, we focused mainly on the lag phase that was determined during the amyloid fibril formation. To do so, we produced several nanopores with a tip diameter adapted to the degree of aggregate maturation, and analysed the Aβ(1-42) species present from a reaction mixture at different times using resistive pulse experiments. The experimental data of current blockades were compared with a theoretical model and with the results of molecular dynamics simulations.

2. Materials and methods

116 **2.1. Aβ(1-42) aggregation and characterization**

117 ***Preparation of monomeric* Aβ*(1-42)***. Aβ(1-42) peptides (ERI Amyloid Laboratory LLC,
118 Oxford, CT,USA)) were maintained in a monomeric state using the protocol described in Serra-
119 Batiste et al. (Serra-Batiste et al., 2016). Briefly, Aβ(1-42) peptides were dissolved in a 6.8 M
120 guanidine thiocyanate solution (Sigma-Aldrich) at a concentration of 8.5 mg mL^{-1}. The solution
121 was then sonicated for 5 min at 52 °C, and diluted with ultrapure water to reach a final
122 concentration of 5 mg mL^{-1} of Aβ(1-42) peptides and 4 M of guanidine thiocyanate. Solution
123 was centrifuged at 10,000 g for 6 min at 4°C. The collected supernatant was filtered (PVDF,
124 0.45 μm) and then injected into a Superdex 75 Increase 10/300GL column (GE Heathcare Life
125 Science) previously equilibrated with 10 mM sodium phosphate buffer pH 7.4. Purification was
126 performed with a 0.5 mL min^{-1} flow to collect the peak attributed to monomeric Aβ(1-42). The
127 Aβ(1-42) peptides concentration was determined with a NanoDrop 8000 spectrophotometer
128 (Thermo Scientific). The aliquots of peptides were stored at -20 °C.

129 ***Preparation and characterization of* Aβ(1-42) *aggregates***. Aβ(1-42) stock solution was
130 diluted to 30 μM in a 10 mM sodium phosphate buffer, pH 7.4 and left to aggregate in low-
131 binding Eppendorf tubes for a final volume of 600 μL. Experiments with pyrimethanil were
132 conducted under the same conditions, except that fungicide was added from a filtered (PVDF,
133 0.22 μm) stock solution to get a 1:15 molar ratio (Aβ(1-42): pesticide), with a final
134 concentration of DMSO of 1% (v/v). To keep the identical conditions, an equal volume of
135 DMSO was added to the control tube. Tubes were arranged vertically and incubated at 25 °C
136 under quiescent state. The fibril formation was monitored by a thioflavin T (ThT) binding assay.
137 Briefly, 20 μL aliquots were withdrawn at specific times and mixed with 14 μL of 142 mM
138 GlyNaOH buffer, pH 8.3 and 6 μL of 100 μM of ThT in a 96-well plate of black polystyrene
139 with a clear bottom coated with a PEG (Thermofisher Scientific). ThT fluorescence of each
140 sample was measured (λex = 445 nm and λem = 485 nm) in a Fluoroskan Ascent microplate

fluorimeter (Thermofisher Scientific). Aggregation profiles were generated with GraphPad Prism software. Curves were fitted using the built-in sigmoidal fit. Each kinetic trace was fitted independently to extract the time required to reach 50% of the maximum fluorescence intensity, known as t_{50}.

2.2. Nanopore production and characterization

Single tracks were produced by Xe irradiation (8.98 MeV u^{-1}) of PET film (6 µm, Goodfellow) at GANIL (SME line, Caen, France). The activation of the track was performed by a UV exposition of 8 h for the tip side and 11 h for the base side (Fisher bioblock; VL215.MC, λ=312 nm) before the chemical etching process. The etching of the conical nanopore was performed under asymmetric conditions as previously reported (Lepoitevin et al., 2016). After the nanopore etching, the film was stabilized overnight in 18 MΩ water. The approximate tip diameter was obtained by conductance measurement. After the chemical etching, the current-voltage (I-V) curve was measured at pH 7. Then the nanopore was functionalized with PEG_{5k}-NH_2 (Nanocs, PG1-AM-5K) using 1-ethyl-3-(-3-dimethylaminopropyl) carbodiimide hydrochloride (EDC, Sigma Aldrich, E7750) as previously reported in order to prevent the unspecific adsorption and improve the nanopore lifetime[35]. The success of the grafting was confirmed by the decrease of I-V curve slope due to the replacement of COO- by the PEG which diminished the diameter of the nanopore (see figure S1). The estimation of nanopore size was performed using quasi-1D model (see supporting information section 1)

2.3. Detection of Aβ(1-42) aggregates using resistive pulse

The nanopore functionalized with PEG moieties was mounted between two compartments of a Teflon cells filled with PBS 1X aqueous solution (pH = 7.2). The Aβ(1-42) at different aggregation times (from 0 to 72 h) in presence or not of pyrimethanil was added to the base side to reach a concentration of 30 nM (monomer equivalent). The resistive pulse experiments were

performed using a patch-clamp amplifier (EPC 10, HEKA electronics, Germany) with Ag/AgCl electrodes. A voltage of 1 V was applied to the working electrode located in the tip side compartment to drive the negatively charged Aβ(1-42), (isoelectric point of 5.5) to pass through the nanopore from the base to the tip side. The ionic currents were recorded at 50 kHz. The signal was filtered at 5 kHz by a Bessel filter. The resistive pulse detection was recorded on the fly. The current traces were further analysed to detect events using lab-made software "Peak Nano Tools" developed using Labview. First the signal was filtered using Butterworth filter 1 kHz order 1. The threshold for the event detection was defined as follows: (i) correct the baseline using a Stavinsky-Golay filter (ii), define the noise levels by the global standard deviation methods (iii) define the threshold. In this work, the threshold has been fixed at about 4σ (where σ is the standard deviation of the signal after baseline correction).

2.4. Molecular dynamic simulation

Description of the protocol Classical all-atom MD simulations were performed using the NAMD.2.12 package(Phillips et al., 2005) . The different systems were solvated in a water box large enough to prevent the interaction between the central part (the conical pore) and its neighbouring periodic cells. KCl ions (at a concentration of 1 M) were added to the water (simulated using the TIP3P model) to reproduce the experimental environment. CHARMM36 (Brooks et al., 2009; Lee et al., 2015) force-field optimization parameters were used in all simulations. During the simulations, the system temperature and pressure were kept constant at 300 K (Langevin dynamics) and 1 atm (Langevin piston), respectively. The long-range electrostatic forces were evaluated using the classical particle mesh Ewald (PME) method with a grid spacing of 1.2 Å, and a fourth-order spline interpolation. The integration time step was equal to 1 fs. Each simulation employed periodic boundary conditions in the three directions of space.

Description of the conical nanopore. To build the conical solid-state nanopore (R_{tip} = 3 nm, R_{base} = 3.5 nm, length=14.8 nm) several carbon nanotube sections of different radii were associated and centred along the nanopore axis. To model the chemical structure of PET nanopore used in the experiments, one third of the carbon atoms constituting the nanopore were randomly configured as oxygen atoms. Partial charges, positive for carbon and negative for oxygen atoms, were added while global neutrality of the nanopore was conserved. Each section was then modified according to the experimental functionalization of the conical nanopore by grafting 30 hydroxyls functions (0.10 M) to randomly picked carbon atoms. Then, three PEG 5K were added (1.15 M), as in the experiments. To place the PEG, a position of linkage was chosen with a random generator number. Nevertheless, to orient each molecule, we took into account the position of each one in order to avoid the superposition of the different structures. Finally, the functionalized nanopore was placed between 2 reservoirs of dimensions equal to 133*133*68 A^3 and solvated with K^+ and Cl^- ions concentration equal to 1 M. The reservoir size was chosen to be around twice the size of the conical-tube part of the nanopore. The complete system dimensions are 133*133*285 $Å^3$, for a total of around 320.000 atoms, detailed as such: 24.000 for the nanopore, 2.400 for PEGs, 3.700 for ions and 290.000 for water. Once the complete functionalized system was obtained, it was optimized following three successive procedures. First, we minimized the energy of the total system at 0 K. Then, the system was progressively heated until reaching a temperature equal to 300 K. Finally, the system was left to evolve at the NPT ensemble, and physical observables were calculated using time averages. During all simulations, every atom constituting the conical nanopore was kept fixed. This system was relaxed for 30 ns, allowing for PEG to relax around the surface of the nanopore. For further computations dealing with ionic current calculations, various electric fields were applied. Those simulations were performed in the NVT ensemble. Once run, the determination of the ionic current was performed according to the procedure described in Ref

(Aksimentiev and Schulten, 2005) by following each ion in the nanopore during its displacement.

Description of the simulated different amyloids. 5OQV/2NAO/2BEG: Three types of Aβ(1-42) amyloid arrangements were generated and studied by simulations. To the previously described 5OQV(Gremer et al., 2017) and 2NAO(Wälti et al., 2016)dual subunit amyloid structure, we also studied a single subunit (PDB id = 2BEG(Lührs et al., 2005)) in order to see its role on the current perturbation inside the nanopore. First, we were interested in the behaviour of small amyloid structures (i.e., 2BEG) in the conical nanopore. Structures used in this case were extracted from RCSB Protein Databank, relaxed in water and 1M KCl ions for 10 ns and then inserted inside the relaxed functionalized nanopore. Once it was shown that simulating translocation under a voltage was possible, we simulated the translocation of the bigger amyloid structures (2NAO and 5OQV). For each simulation run, the relaxed 2NAO or 5OQV was placed at the entrance of the previously described functionalized nanopore, free of water and ions. Water and ions were then added into the systems and relaxed. Note that for the relaxed 2BEG amyloid, we started the simulation with the amyloid inside the nanopore.

3. Result and discussion

3.1. Impact of pyrimethanil on the aggregation

The aggregation kinetics starting from pure monomeric Aβ(1-42) was characterized by using the reporter dye thioflavin T, which undergoes an enhancement of quantum yield when bound to β-sheet structure of fibrils (Figure 1A). The addition of pyrimethanil efficiently accelerated the reaction by decreasing to 50% the half-time of aggregation (t_{50}) (from about 122 to 66 hours). The fluorescence intensity of ThT at the post-transition plateau in the presence of pyrimethanil was significantly higher (about a two-fold increase), compared to that obtained using Aβ(1-42) fibrils alone. This supports the idea that pyrimethanil facilitates a conformational rearrangement leading to different fibril morphotypes. However, no major

macrostructural changes induced by pyrimethanil treatment were revealed by transmission electron microscopy (Figure 1b-c).

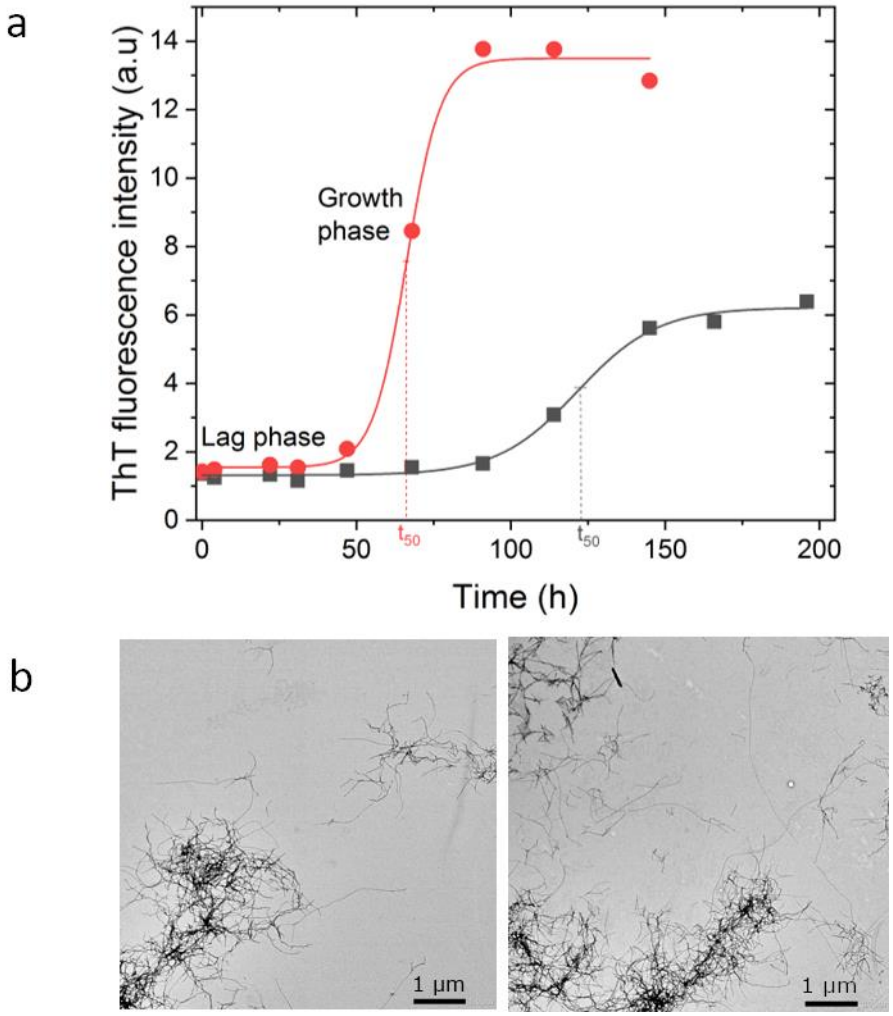

Figure 1: Effect of pyrimethanil on the kinetics of Aβ fibrils formation. (a) Aβ(1-42) monomers (30 µM) were incubated with pyrimethanil (750 µM) (red curve), or with an equivalent volume of DMSO (1%) (black curve) with a ratio 1:15. ThT fluorescence intensity was measured once a day (a.u., arbitrary units). The different values obtained were plotted. The sigmoidal fits were done using Boltzmann equation ($I = I_0 + (I_0 - I_F)/1 + \exp(t_{50} - t/a)$) where I, I_0 and I_F are the fluorescence intensity at time t, at the initial and final plateaus respectively, and t_{50} the half-time of aggregation. (b) Negative-stained transmission electron micrographs of Aβ(1-42) fibrils formed in the absence (left panel) or presence (right panel) of pyrimethanil.

3.2. Investigation of the lag phase using nanopore

To further characterize the pro-aggregating effect of pyrimethanil on Aβ(1-42) during the lag phase of amyloidogenesis the aliquots were withdrawn at different time intervals and analysed using conical track-etched nanopores. To do so, we used a conical nanopore functionalized with PEG as previously reported(Giamblanco et al., 2018a). The characterization of nanopore using quasi-1D model for pore resistance gives a pore tip radius $r_t \sim 4.7$ nm while the pore base radius $r_b = 170$ nm was determined by SEM (See Supplementary Information S1). The detection of Aβ(1-42) aggregates was performed using resistive pulse methods from the base to the tip side (Figure 2a). From the current traces, we detected events characterized by the relative current blockade noted $\Delta I/I_0$, the dwell time Δt, both the left and right slope and the variance of the close current (Figure 2b). In Figure 2, the current trace recorded for Aβ(1-42) at various incubation times (from 4 h to 72 h) with pyrimethanil or not are reported. First, we observed the current blockade for all the samples. This means that after 4h in presence or absence of pyrimethanil, Aβ(1-42) aggregates are detected. The zoom of certain current blockades reveals large fluctuations of the closed current levels that can be assigned to the reorientation of an aggregate inside the detection zone of the nanopore. During the experiment, we also observe events where the base line level is not reached while the event is supposed to be finished (see figure 2 d, orange line). This could have two interpretations (i) an aggregate is adsorbed close to the narrow aperture or (ii) a large aggregate is trapped inside the nanopore. Because the origin of such events is not clear, we did not consider these events in the further analysis. For each event, we analysed both the left and the right slope (see SI-2, figure S3). For all recorded events, the values of the left slope corresponding to the beginning of the event are one order of magnitude larger than the right one that corresponds to the aggregate exit from the nanopore. Such dissymmetry is a typical feature of the track-etched nanopore presenting a conical shape.

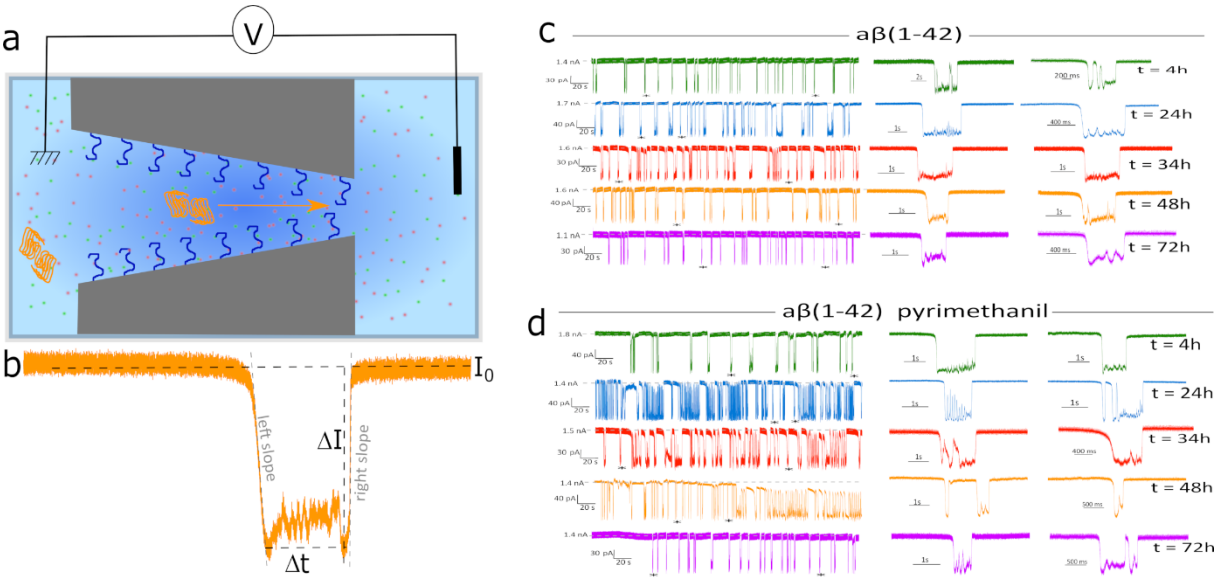

Figure 2: (a) Sketch of nanopore experiments. Aβ(1-42) after incubation 72 h with and without pyrimethanil (b) illustration of the parameters measured for each current blockade. Examples of current traces recorded during resistive pulse experiments for Aβ(1-42) after incubation without (c) and with pyrimethanil (d) for various times. The experiments were performed using nanopore $r_t = \sim 4.7$ nm. On the right side, example of current blockade is reported.

From the current traces, we detected events characterized by the relative current blockade noted $\Delta I/I_0$ and the dwell time Δt. In Figure 3, both the distribution of $\Delta I/I_0$ and the event map recorded for Aβ(1-42) after 4 h, 24 h, 34 h, 48 h, 72 h, incubation without or with pyrimethanil are reported. Without pyrimethanil and after 4h, the distribution is bimodal centred to 0.90 and 0.94±0.04 evidencing the presence of two distinct populations in the sample. After 24h, the distribution becomes monomodal centred to 0.90±0.04. Interestingly, the larger $\Delta I/I_0$ distribution disappears. This result is counter-intuitive. Indeed, we expected that with time the aggregate should be larger. However, we observe an increase of the dwell time distribution (Figure SI-5). This means that the assemblies occupy less space inside the nanopore but translocate more slowly. This suggests at this stage a reorganization of the aggregate. After 34h and 48h, we observe that the amplitude of the relative current blockade increases and their distribution is wider (0.92±0.06 and 0.93±0.06 respectively). In addition, the distribution of the

dwell time is more spread and reveal two clusters. The first population exhibits a dwell time> 105 ms, while the second one is spread from 110 ms to 2500 ms. This suggests that the population of oligomers is more and more heterogeneous. After 72 h, the $\Delta I/I_0$ distribution is shaper, reaching 0.95±0.04. On the other hand, the dwell time distribution is also more compact since only one population is obtained. Concerning the distribution of $\Delta I/I_0$ and the events map for the for Aβ(1-42) incubated in presence of pyrimethanyl we can report that after 4 h of incubation, the distribution of $\Delta I/I_0$ is centred to 0.90±0.04. After 24 h and 34 h, the distributions $\Delta I/I_0$ are wider and centred 0.94±0.06 and 0.94±0.09. We also observe that the dwell times distributions are more spread, suggesting heterogeneity in the sample. However, compared to the sample without pyrimethanyl, the presence of two distinct populations of dwelling time is not evidenced. After 48 h, the distribution centre of $\Delta I/I_0$ decreases to 0.88±0.06. On the other hand, the dwell time distribution is centred to lower values. This clearly evidences the presence of smaller assemblies. It is interesting to notice that 48 h corresponds to the beginning of the growth phase (figure 1a) determined by the ThT test. After 72 h, the aggregation process is clearly under the growth phase, the distribution shifts toward larger value of $\Delta I/I_0$ (0.93±0.07) and longer dwell time. Our nanopore experiments reveal that the evolution of the population of Aβ(1-42) follows two different trends. Without the pyrimethanyl, after the reorganization occurring between 4 h and 24 h, the Aβ(1-42) aggregates are more and more polydispersed with the incubation time. This is also the case for the sample incubated with pyrimethanyl before the starting of the growth phase where the aggregate structures become more ordered adopting a β-sheet organization. After 48 h of incubation with pyrimethanyl, the presence of smaller assemblies revealed by nanopore experiments is consistent with a quaternary structural convergence, by reducing the parental polydispersity, and generation of smaller assemblies. These results led us to conclude that conformational rearrangements and protomer exchanges,

i.e., dissociation/association events, take place within the initial heterogeneous population of assemblies(Dear et al., 2020b; Dear et al., 2020a; Michaels et al., 2020).

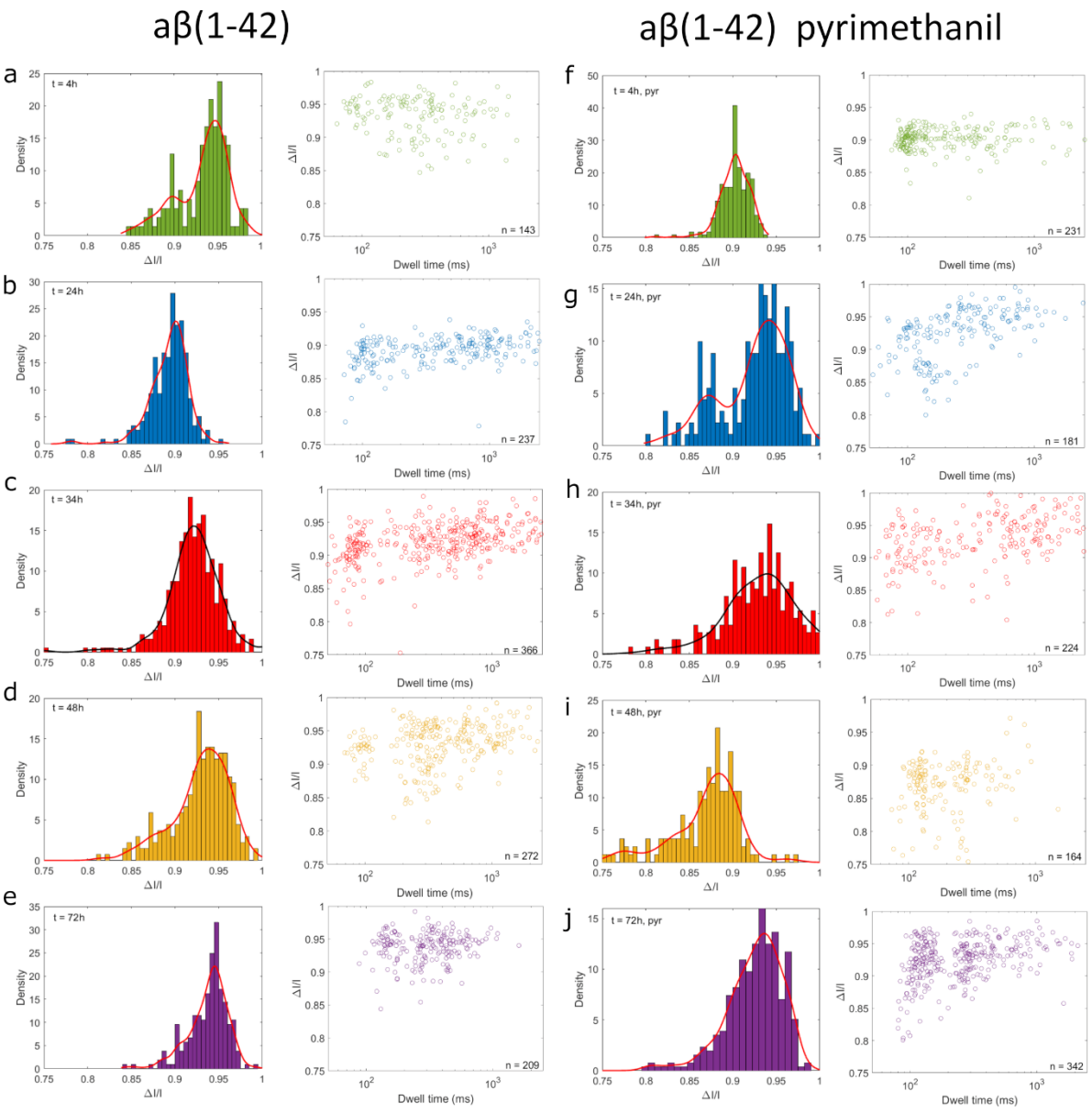

Figure 3: histograms of relative current blockade without (a-e) and with pyrimethanil (f-j) and corresponding event maps of current blockade parameters induced by Aβ(1-42) after various incubation time (4 h green, 24 h blue, 34 h red, 48 h orange, 72 h violet), the lines are the fit using nonparametric law to evaluate the centre of the distribution. The experiments were performed using nanopore r_t = 4.7 nm.

We then performed a theoretical analysis of the expected blockage to estimate the size of Aβ(1-42) aggregate. In general, the current blockade induced by a particle dwelling into a nanopore depends on the particle size, shape, position, orientation, surface charge and

electrolyte solution (Houghtaling et al., 2018a). In nanofluidic systems, different theoretical/computational techniques are commonly used to describe the current blockade and the translocation process (Chinappi and Cecconi, 2018; Qiu et al., 2016). Here, we start our analysis using a theoretical model while in the next section, we discuss molecular dynamics simulations.

One evidence shown in Fig 2 is that the current blockades are always relatively high, i.e. $\Delta I/I_0 \simeq 0.85 - 0.95$. Two questions naturally arise, i) what is the shape of the amyloid aggregates responsible for such high blockades? and ii) why, despite the expected polydispersity of the sample (in a growing process, we expect that different populations, from monomers to large aggregates are present simultaneously) small blockades (e.g., $\Delta I/I_0 > 0.7$) are not observed?

To answer to these questions we employed a quasi-1D model that allows estimating current blockades associated with the presence of a particle partially blocking the pore(DeBlois and Bean, 1970; Di Muccio et al., 2019; Giamblanco et al., 2018a). Assuming that the aggregates have a spherical shape with radius r_a, our model predicts that the blockade ($\Delta I/I_0 \simeq 0.85 - 0.95$) are due to aggregate radii close to the nanopore tip radius, i.e. $r_a \simeq r_t$, see section 3 of SI for details on the physical model. This answers to the first question: the experimentally observed blockades correspond to particles of radius $r_a > 4.5$ nm that occupies the pore tip. The present model is developed for spheres, similar analytic results can be obtained for other simple shapes (e.g. short cylinders or ellipses). The different peaks observed experimentally (see e.g. figure 2a or figure 2g) can be ascribed to particles with slighly different shape and size.

Moreover our model predicts that amyloid aggregates with smaller radius would result in much smaller blockades, e.g., an aggregate of radius 4 nm would gives $\Delta I/I_0 \simeq 0.2$. In principle, such blockade should be detected by our nanopore sensing system. Hence, the fact that such small blockades are not observed deserve an additional explanation. In our opinion,

the most reasonable explanation is that such small aggregates exist in the solution and they actually translocate through the pore. However their translocation is so fast that the signal is not recorded. To support this interpretation, we estimate the dwell time of an aggregate as a function of its radius, see section S4 of SI. The dwell time predicted using only electrophoresis as driving force is much smaller than the observed one. This implies that aggregates are further slowed down by interaction with the pore wall. This interaction is effective only for aggregate of the same size of the pore tip. In summary, our model suggests the following interpretation: aggregates of different sizes are present in the solution. The ones are smaller than the pore tip, $r_a < r_t$, translocate too fast to be detected. The ones have a size similar to the pore, $r_a \sim r_t$, are slowed down by the interaction with pore tip wall and they provide an almost complete blocking of the current $\Delta I/I_0 > 0.85$. Larger aggregates, $r_a > r_t$, could exist in the solution and the resulting blockage would be even larger. Nevertheless, the analysis of the left and right slopes of the blockade events suggest that all the events are associated to translocations (see Figure 2 and Fig S2). Consequently, larger aggregates probably bump at the pore surfaces without reaching the sensing region.

In the light of this interpretation, the pore can also be used as a counter for aggregate of size $r_a \simeq r_t$. The event frequency is reported in Figure 4. In the lag phase $t < 40$h, the event frequency increases with time as expected in an aggregation process. This increase is slightly more pronounced in the experiments with pyrimethanil, suggesting a possible positive effect of pyrimethanil in the first phase of aggregation, coherently with the fluorescence data in Figure 1. With pyrimethanyl, we observe a decrease of the capture rate at 48 h of incubation. This can be explained by a decrease of the aggregate size and thus a part of these aggregates would become too small to be detected by nanopore. Interestingly, the evolution of the capture rate and the size of aggregate suggest that the pyrimethanyl induce a mechanism of aggregation in two steps due to a reorganization and/or fragmentation phenomena.

At this stage, several questions are still open to draw a complete description of the current blockade. Indeed, we found that the dwell time is long (until second scale) and the origin of the fluctuation occurring during the aggregate translocation is not fully understood. We plot in Fig. S4 the relation between the standard deviation of the current blockade vs the dwell time for each event. First, we can observe that the dispersion of the standard deviation increases with the dwell time evidencing that the fluctuation occurs more often during the long event. Second, the disparity of the standard deviation seems dependent on the incubation time and the presence of pyrimethanyl. Typically, for the sample incubated without pyrimethanil, it is narrow after 72 h incubation while in presence of pyrimethanil, it becomes narrow after 48 h. The latter could be concomitant with the apparition of ordered β-sheet structure. This is in accordance with a mechanism of aggregation in two steps suggested by the evolution capture rate and the $\Delta I/I_0$.

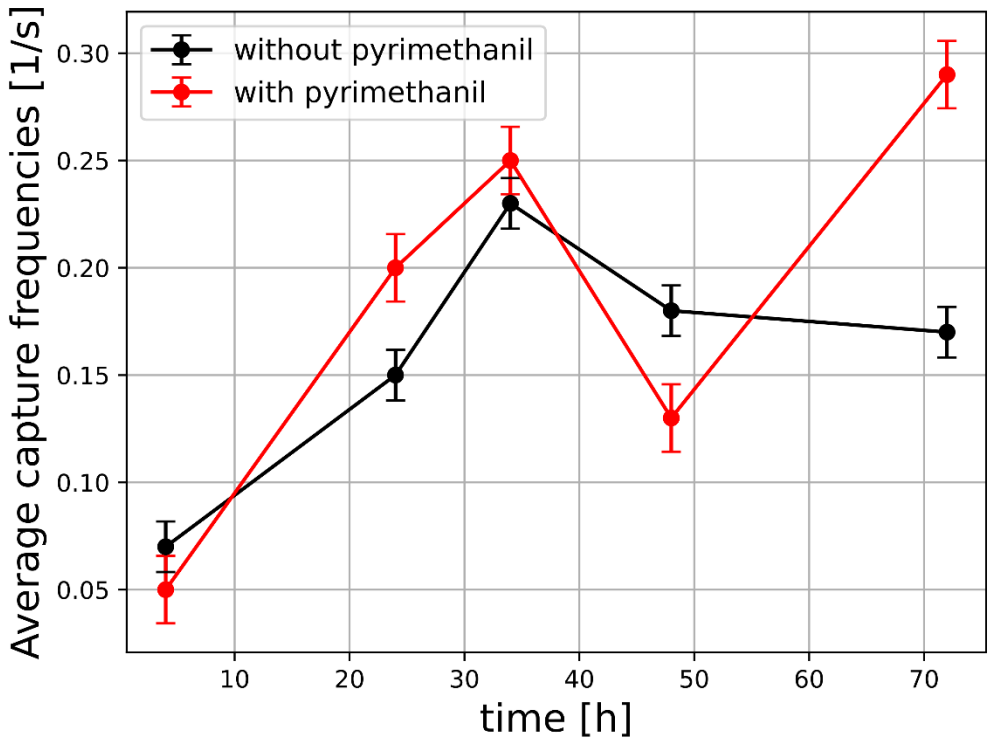

Figure 4: Average capture frequency for each experiment with (red curve) and without (black curve) pyrimethanil.

3.3. Molecular dynamic simulation

To provide additional insights on the Aβ(1-42) aggregate translocation through the nanopore, we use molecular dynamic simulations. We aim to demonstrate that the interaction between the nanopore and the aggregate is strongly depending on their structure. For this, we choose different Aβ(1-42) aggregates from the PBD even if they are not strictly identical to the experimental one. First, we studied the interaction between the nanopore and the Aβ(1-42) aggregate with a single subunit structure (PDB-id 2BEG) (see Supplementary Information S5 and Video_S1), before generalizing this approach to the larger systems (2NAO and 5OQV PDB structures, respectively) (Fig. 5). We notice that the nanopore is smaller than the experimental one (r_t = 3 nm while r_t = 4.7) to keep a reasonable simulation box.

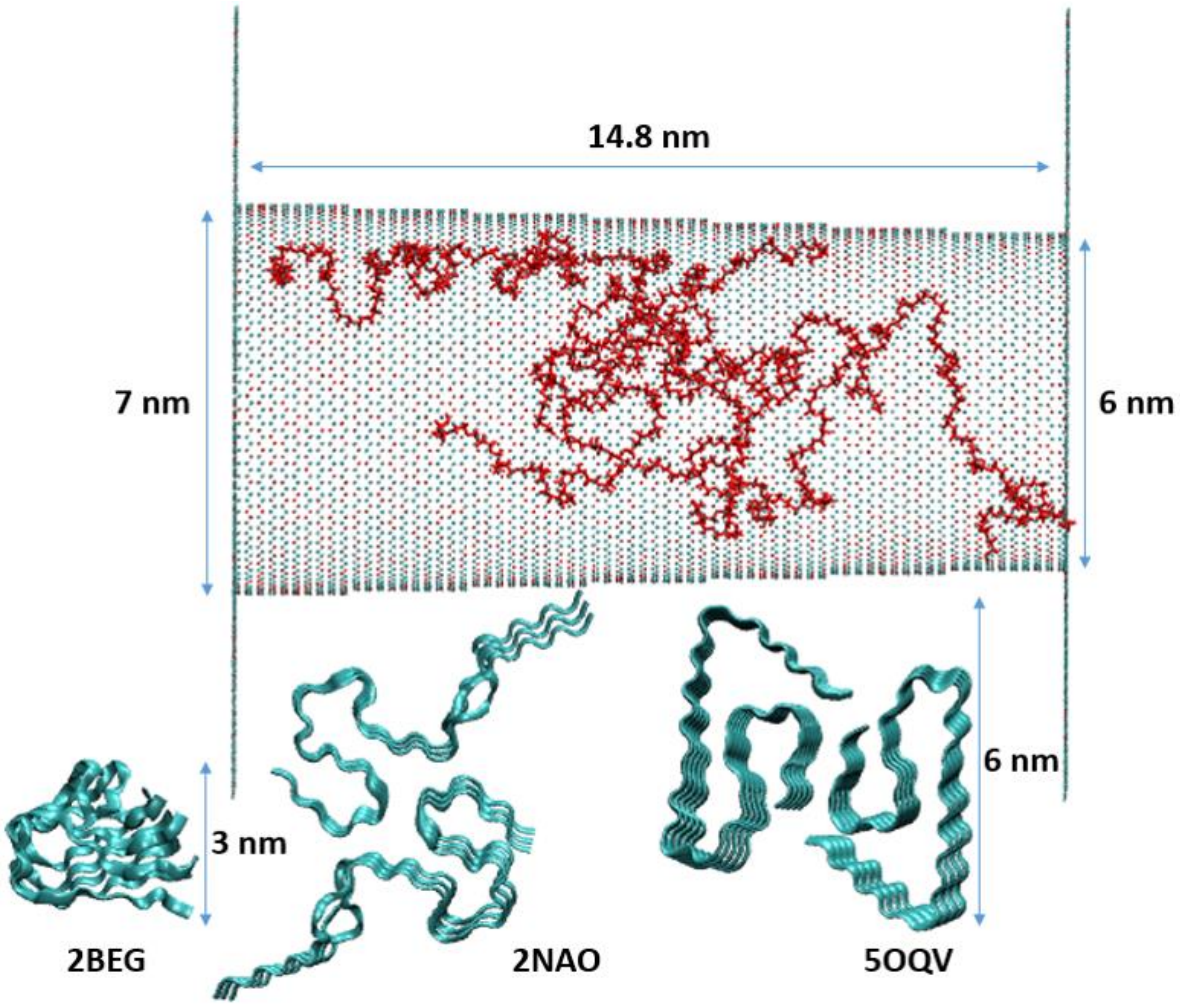

Figure 5. Snapshots of different elements of the simulations at full scale. Top: functionalized nanopore. Bottom from left to right: 2BEG, 2NAO and 5OQV fibrils in ribbon representation.

The translocation of the different fibril structures in the nanopore was investigated for two voltages (0.2 V and 2 V, electric field oriented from tip to base). Under 0.2 V, we did not observe Aβ(1-42) aggregate displacement (see Supplementary Information S5). Thus, we focused our studies at a higher voltage (2 V). The translocation does not exhibit a smooth and linear behaviour as shown in Figure 6. We note here that some of our attempts led to different phenomena than expected. Our attempt with 2NAO (see video_S3) led to the protein adsorption on the nanopore. After ~11 ns of stability (plateau in Figure 6), the protein splits itself in two subunits with one resuming translocation while the other stays adsorbed. The 5OQV protein did not adopt the same behaviour, since no splitting has been observed during its translocation (see video_S4 and video_S6). Note that these observations are, of course, heavily dependent on the entrance's radius and of the PEG conformation.

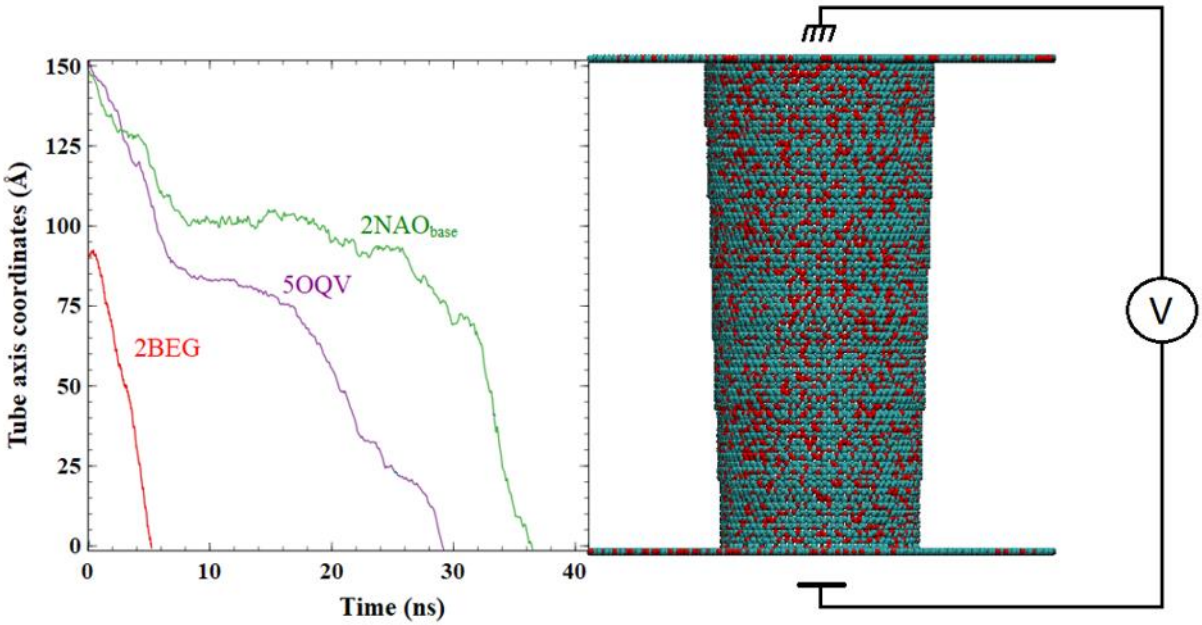

Figure 6: Position of each protein's mass centre over the axis of the nanopore. The base entrance of the nanopore is positioned at coordinate 148.4 Å whereas tip entrance is situated at 0 Å.

Once the translocation was achieved, we extracted from simulations the 1-D speed of each mass centre of protein along the nanopore axis in order to compute the average speed and to observe the different behaviours over the translocation (**Table 1**).

Table 1: Translocation events of 5OQV, 2NAO and 2BEG in the different tested configurations. The translocation duration and the average speed of the protein were obtained through the analysis of Figure 6. Current blockades were computed using the analysis of the ions displacements.

Base entrance	Translocation Duration	Average speed	Number of monomer chains (sub-units)
5OQV	27 ns	0.52 m s-1	9 (2)
2NAO	37 ns	0.41 m s-1	6 (2)
2BEG	4.6 ns	1.98 m s-1	5

When inserted from the base entrance, 5OQV and 2NAO translocation shows some sort of similarity. Both proteins adsorb around the base of the nanopore, with less PEG coating on its surface, for respectively ~8 and ~11 ns. Before and after the adsorption, we observe a quasi-linear progression inside the nanopore. 5OQV enters faster in the base part than when it travels through the tip part (speeds equal to 0.82 m s^{-1} and 0.53 m s^{-1} respectively, see Supplementary Information S6). This can be explained by its difficulty to leave through the smaller tip radius, its interaction with the PEG coating and the loss of its momentum while adsorbed. 2NAO shows the opposite, with a speed of 0.58 m s^{-1} in the base part and a speed equal to 0.81 m s^{-1} in the tip part. It has to be noted that the tip part speed is only for half the protein, as 2NAO splits during the translocation. This resulted thus from possible interactions with the nanopore wall and the PEG during the translocation of the proteins. Note that we also extracted the same

information for the previously described 2BEG system under a 2 V voltage which could be compared to other proteins. We can thus compare speed for the last ~8 nm, after all three proteins had been desorbed from the nanopore. For 5OQV (5643 atoms), half 2NAO (1881 atoms) and 2BEG (1870 atoms), we obtain respective speeds of 0.53 m s^{-1}, 0.81 m s^{-1} and 1.98 m s^{-1}. These velocities at high-voltage lead to translocation times that are still smaller than experiments (27 ns, 37 ns and 4.6 ns, respectively).

Even if the molecular dynamic simulation was not performed under strictly the same condition as the experiments. The results allow providing elements to better understand the long dwell time. Indeed, as described in Supplementary Information, at low voltage (0.2 V), the interaction of the protein with the functionalized nanopore remained so high that no net displacement of the Aβ(1-42) aggregate was observed. The adhesion of the protein, under the combined effect of a longer nanopore and a lower induced voltage, seems thus to have a crucial role in the amyloid dwell time as suggested by the different simulation conditions. In addition, the simulation highlights a slowdown of the Aβ(1-42) aggregate when it reaches the PEG chain. Thus, it is plausible that similar scenario occurs inside conical nanopore , explaining long dwell time experimentally observed. According to theoretical conclusion, we could speculate that the small aggregate does not enter in interaction with the PEG and thus translocate faster (no event is observed), conversely the aggregate that reaches a critical size promoting a strong interaction with PEG is detected.

4. Conclusions

Our work aimed to investigate the effect of pyrimethanil on Aβ(1-42) aggregation. Using conical nanopores functionalized with PEG, we successfully detected Aβ(1-42) aggregates at different time during the lag phase where the oligomer are often too small to be detected by other techniques. Regardless the incubation time and the presence of pyrimethanil, long large current (>0.7) blockades are observed. Using an analytical model only based on geometrical

consideration, we could assign the detectable events to the Aβ(1-42) aggregates with a size close to that of the sensing pore diameter. The molecular dynamic simulations confirm that the Aβ(1-42) aggregates can translocate through the nanopore but interact with PEG explaining the long dwell time (hundreds ms scale) experimentally recorded. They also evidence amyloid/pore interaction in the zone without PEG coating confirming its importance. Such interaction let think splitting phenomena of the dimer structure occurs. The Aβ(1-42) aggregates interaction with PEG and the uncoated zones will make the experimentalist to optimize the antifouling functionalization.

Generally speaking, by combining conventional techniques and single nanopore-based technology, our work confirms pyrimethanil as an enhancer of Aβ(1-42) assembly during the lag phase of fibril formation. More interestingly, the nanopore approach evidences that the pyrimethanil induce an aggregation of Aβ(1-42) mechanism in two steps including the reorganization after 48 h at the beginning of the elongation phase. This supports the emerging theory that the fibril formation involved numerous phases of dissociation, conversion and fragmentation. The original result here is that such phenomena can occur quickly in presence of pyrimethanil. This opens numerous questions about the health impact of certain chemicals used in agriculture.

Acknowledgements

This work was founded by Agence Nationale de la Recherche (ANR-19-CE42-0006, NanoOligo). MB, SB and MC acknowledge l'Università Italo Francese and Campus France through Galileo (project G16-173) and Vinci (project C3-1352) grants. Single tracks have been produced in GANIL (Caen, France) in the framework of an EMIR project. The authors thank E. Balanzat for the assistance at GANIL. Calculations were performed at the supercomputer regional facility Mesocentre of the University of Franche-Comté with the assistance of K. Mazouzi. This work was also granted access to the HPC resources of IDRIS, Jean Zay

supercomputer, under the allocation 2019 - DARI A0070711074 made by GENCI. Finally, part of this work was performed using computing resources of CRIANN (Normandy, France).

References

Aksimentiev, A., Schulten, K., 2005. Imaging α-Hemolysin with Molecular Dynamics: Ionic Conductance, Osmotic Permeability, and the Electrostatic Potential Map. Biophysical Journal, 88(6), 3745-3761. Biophysical journal 88 (6), 3745–3761. doi:10.1529/biophysj.104.058727.

Asandei, A., Iftemi, S., Mereuta, L., Schiopu, I., Luchian, T., 2014. Probing of Various Physiologically Relevant Metals–Amyloid-β Peptide Interactions with a Lipid Membrane-Immobilized Protein Nanopore. J Membrane Biol 247 (6), 531. doi:10.1007/s00232-014-9667-7.

Asandei, A., Rossini, A.E., Chinappi, M., Park, Y., Luchian, T., 2017. Protein Nanopore-Based Discrimination between Selected Neutral Amino Acids from Polypeptides. Langmuir 33 (50), 14451–14459. doi:10.1021/acs.langmuir.7b03163.

Asandei, A., Schiopu, I., Iftemi, S., Mereuta, L., Luchian, T., 2013. Investigation of Cu2+ binding to human and rat amyloid fragments Aβ (1-16) with a protein nanopore. Langmuir : the ACS journal of surfaces and colloids 29 (50), 15634–15642. doi:10.1021/la403915t.

Balme, S., Coulon, P.E., Lepoitevin, M., Charlot, B., Yandrapalli, N., Favard, C., Muriaux, D., Bechelany, M., Janot, J.-M., 2016. Influence of Adsorption on Proteins and Amyloid Detection by Silicon Nitride Nanopore. Langmuir : the ACS journal of surfaces and colloids 32 (35), 8916–8925. doi:10.1021/acs.langmuir.6b02048.

Bonome, E.L., Cecconi, F., Chinappi, M., 2019. Translocation intermediates of ubiquitin through an α-hemolysin nanopore: implications for detection of post-translational modifications. NANOSCALE 11 (20), 9920–9930. doi:10.1039/c8nr10492a.

512 Brooks, B.R., Brooks III, C.L., Mackerell Jr, A.D., Nilsson, L., Petrella, R.J., Roux, B., Won,
513 Y., Archontis, G., Bartels, C., Boresch, S., 2009. CHARMM: the biomolecular simulation
514 program. Journal of computational chemistry 30 (10), 1545–1614.
515 Carulla, N., Zhou, M., Giralt, E., Robinson, C.V., Dobson, C.M., 2010. Structure and
516 intermolecular dynamics of aggregates populated during amyloid fibril formation studied
517 by hydrogen/deuterium exchange. Accounts of chemical research 43 (8), 1072–1079.
518 doi:10.1021/ar9002784.
519 Chau, C.C., Radford, S.E., Hewitt, E.W., Actis, P., 2020. Macromolecular Crowding
520 Enhances the Detection of DNA and Proteins by a Solid-State Nanopore. Nano letters 20
521 (7), 5553–5561. doi:10.1021/acs.nanolett.0c02246.
522 Chinappi, M., Cecconi, F., 2018. Protein sequencing via nanopore based devices: a
523 nanofluidics perspective. Journal of Physics: Condensed Matter, 30(20), 204002. J. Phys.:
524 Condens. Matter 30 (20), 204002. doi:10.1088/1361-648X/aababe.
525 Chin-Chan, M., Navarro-Yepes, J., Quintanilla-Vega, B., 2015. Environmental pollutants as
526 risk factors for neurodegenerative disorders: Alzheimer and Parkinson diseases. Front.
527 Cell. Neurosci. 9, 124. doi:10.3389/fncel.2015.00124.
528 Chiti, F., Dobson, C.M., 2017. Protein Misfolding, Amyloid Formation, and Human Disease:
529 A Summary of Progress Over the Last Decade. Annual review of biochemistry 86, 27–68.
530 doi:10.1146/annurev-biochem-061516-045115.
531 Coglitore, D., Coulon, P.E., Janot, J.-M., Balme, S., 2019. Revealing the Nanoparticle-Protein
532 Corona with a Solid-State Nanopore. Materials (Basel, Switzerland) 12 (21).
533 doi:10.3390/ma12213524.
534 Coglitore, D., Giamblanco, N., Kizalaité, A., Coulon, P.E., Charlot, B., Janot, J.-M., Balme,
535 S., 2018. Unexpected Hard Protein Behavior of BSA on Gold Nanoparticle Caused by

536 Resveratrol. Langmuir : the ACS journal of surfaces and colloids 34 (30), 8866–8874.
537 doi:10.1021/acs.langmuir.8b01365.
538 Dear, A.J., Meisl, G., Šarić, A., Michaels, T.C.T., Kjaergaard, M., Linse, S., Knowles, T.P.J.,
539 2020a. Identification of on- and off-pathway oligomers in amyloid fibril formation.
540 CHEMICAL SCIENCE 11 (24), 6236–6247. doi:10.1039/c9sc06501f.
541 Dear, A.J., Michaels, T.C.T., Meisl, G., Klenerman, D., Wu, S., Perrett, S., Linse, S., Dobson,
542 C.M., Knowles, T.P.J., 2020b. Kinetic diversity of amyloid oligomers. Proceedings of the
543 National Academy of Sciences of the United States of America 117 (22), 12087–12094.
544 doi:10.1073/pnas.1922267117.
545 DeBlois, R.W., Bean, C.P., 1970. Counting and Sizing of Submicron Particles by the
546 Resistive Pulse Technique. Review of Scientific Instruments 41 (7), 909–916.
547 doi:10.1063/1.1684724.
548 Di Marino, D., Bonome, E.L., Tramontano, A., Chinappi, M., 2015. All-Atom Molecular
549 Dynamics Simulation of Protein Translocation through an α-Hemolysin Nanopore. The
550 Journal of Physical Chemistry Letters, 6(15), 2963-2968. The Journal of Physical
551 Chemistry Letters 6 (15), 2963–2968. doi:10.1021/acs.jpclett.5b01077.
552 Di Muccio, G., Rossini, A.E., Di Marino, D., Zollo, G., Chinappi, M., 2019. Insights into
553 protein sequencing with an α-Hemolysin nanopore by atomistic simulations. Sci Rep 9 (1),
554 6440. doi:10.1038/s41598-019-42867-7.
555 Gazit, E., 2002. The "Correctly Folded" state of proteins: is it a metastable state? Angewandte
556 Chemie (International ed. in English) 41 (2), 257–259. doi:10.1002/1521-
557 3773(20020118)41:2<257:aid-anie257>3.0.co;2-m.
558 Giamblanco, N., Coglitore, D., Gubbiotti, A., Ma, T., Balanzat, E., Janot, J.-M., Chinappi, M.,
559 Balme, S., 2018a. Amyloid Growth, Inhibition, and Real-Time Enzymatic Degradation

560 Revealed with Single Conical Nanopore. Analytical chemistry 90 (21), 12900–12908.
561 doi:10.1021/acs.analchem.8b03523.
562 Giamblanco, N., Coglitore, D., Janot, J.-M., Coulon, P.E., Charlot, B., Balme, S., 2018b.
563 Detection of protein aggregate morphology through single antifouling nanopore. Sensors
564 and Actuators B: Chemical 260, 736–745. doi:10.1016/j.snb.2018.01.094.
565 Giamblanco, N., Fichou, Y., Janot, J.-M., Balanzat, E., Han, S., Balme, S., 2020a.
566 Mechanisms of Heparin-Induced Tau Aggregation Revealed by a Single Nanopore. ACS
567 sensors 5 (4), 1158–1167. doi:10.1021/acssensors.0c00193.
568 Giamblanco, N., Janot, J.-M., Gubbiotti, A., Chinappi, M., Balme, S., 2020b. Characterization
569 of Food Amyloid Protein Digestion by Conical Nanopore. Small Methods 9, 1900703.
570 doi:10.1002/smtd.201900703.
571 Gremer, L., Schölzel, D., Schenk, C., Reinartz, E., Labahn, J., Ravelli, R.B.G., Tusche, M.,
572 Lopez-Iglesias, C., Hoyer, W., Heise, H., Willbold, D., Schröder, G.F., 2017. Fibril
573 structure of amyloid-β(1-42) by cryo-electron microscopy. Science (New York, N.Y.) 358
574 (6359), 116–119. doi:10.1126/science.aao2825.
575 Hayden, K.M., Norton, M.C., Darcey, D., Ostbye, T., Zandi, P.P., Breitner, J.C.S., Welsh-
576 Bohmer, K.A., 2010. Occupational exposure to pesticides increases the risk of incident
577 AD: the Cache County study. Neurology 74 (19), 1524–1530.
578 doi:10.1212/WNL.0b013e3181dd4423.
579 Houghtaling, J., List, J., Mayer, M., 2018a. Nanopore-Based, Rapid Characterization of
580 Individual Amyloid Particles in Solution: Concepts, Challenges, and Prospects. SMALL
581 14 (46, SI). doi:10.1002/smll.201802412.
582 Houghtaling, J., List, J., Mayer, M., 2018b. Nanopore-Based, Rapid Characterization of
583 Individual Amyloid Particles in Solution: Concepts, Challenges, and Prospects. Small

(Weinheim an der Bergstrasse, Germany) 14 (46), e1802412. doi:10.1002/smll.201802412.

Hu, R., Diao, J., Li, J., Tang, Z., Li, X., Leitz, J., Long, J., Liu, J., Yu, D., Zhao, Q. Intrinsic and membrane-facilitated α-synuclein oligomerization revealed by label-free detection through solid-state nanopores. Sci Rep 6 (1), 1–11. doi:10.1038/srep20776.

Huang, G., Voet, A., Maglia, G., 2019. FraC nanopores with adjustable diameter identify the mass of opposite-charge peptides with 44 dalton resolution. Nature communications 10 (1), 835. doi:10.1038/s41467-019-08761-6.

Jahn, T.R., Radford, S.E., 2008. Folding versus aggregation: polypeptide conformations on competing pathways. Archives of biochemistry and biophysics 469 (1), 100–117. doi:10.1016/j.abb.2007.05.015.

Ke, P.C., Zhou, R., Serpell, L.C., Riek, R., Knowles, T.P.J., Lashuel, H.A., Gazit, E., Hamley, I.W., Davis, T.P., Fändrich, M., Otzen, D.E., Chapman, M.R., Dobson, C.M., Eisenberg, D.S., Mezzenga, R., 2020. Half a century of amyloids: past, present and future. Chem. Soc. Rev. 49 (15), 5473–5509. doi:10.1039/c9cs00199a.

Lafon, P.-A., Wang, Y., Arango-Lievano, M., Torrent, J., Salvador-Prince, L., Mansuy, M., Mestre-Francès, N., Givalois, L., Liu, J., Mercader, J.V., Jeanneteau, F., Desrumaux, C., Perrier, V., 2020. Fungicide Residues Exposure and β-amyloid Aggregation in a Mouse Model of Alzheimer's Disease. Environmental health perspectives 128 (1), 17011. doi:10.1289/EHP5550.

Lee, J., Cheng, X., Swails, J.M., Yeom, M.S., Eastman, P.K., Lemkul, J.A., Wei, S., Buckner, J., Jeong, J.C., Qi, Y., Jo, S., Pande, V.S., Case, D.A., Brooks, C.L., MacKerell, A.D., Klauda, J.B., Im, W., 2015. CHARMM-GUI Input Generator for NAMD, GROMACS, AMBER, OpenMM, and CHARMM/OpenMM Simulations Using the CHARMM36 Additive Force Field. Journal of Chemical Theory and Computation, 12(1), 405-413.

609 Journal of Chemical Theory and Computation 12 (1), 405–413.
610 doi:10.1021/acs.jctc.5b00935.
611 Lepoitevin, M., Jamilloux, B., Bechelany, M., Balanzat, E., Janot, J.-M., Balme, S., 2016.
612 Fast and reversible functionalization of a single nanopore based on layer-by-layer
613 polyelectrolyte self-assembly for tuning current rectification and designing sensors. RSC
614 Adv. 6 (38), 32228–32233. doi:10.1039/C6RA03698H.
615 Lepoitevin, M., Ma, T., Bechelany, M., Janot, J.-M., Balme, S., 2017. Functionalization of
616 single solid state nanopores to mimic biological ion channels: A review. Advances in
617 colloid and interface science 250, 195–213. doi:10.1016/j.cis.2017.09.001.
618 Lührs, T., Ritter, C., Adrian, M., Riek-Loher, D., Bohrmann, B., Döbeli, H., Schubert, D.,
619 Riek, R., 2005. 3D structure of Alzheimer's amyloid-beta(1-42) fibrils. Proceedings of the
620 National Academy of Sciences of the United States of America 102 (48), 17342–17347.
621 doi:10.1073/pnas.0506723102.
622 Ma, T., Janot, J.-M., Balme, S., 2020. Track-Etched Nanopore/Membrane: From Fundamental
623 to Applications. Small Methods, 2000366. doi:10.1002/smtd.202000366.
624 Madampage, C., Tavassoly, O., Christensen, C., Kumari, M., Lee, J.S., 2012. Nanopore
625 analysis: An emerging technique for studying the folding and misfolding of proteins. Prion
626 6 (2), 116–123. doi:10.4161/pri.18665.
627 Martyushenko, N., Bell, N.A.W., Lamboll, R.D., Keyser, U.F., 2015. Nanopore analysis of
628 amyloid fibrils formed by lysozyme aggregation. The Analyst 140 (14), 4882–4886.
629 doi:10.1039/c5an00530b.
630 McLaurin, J., Yang, D.-S., Yip, C.M., Fraser, P.E., 2000. Review: Modulating Factors in
631 Amyloid-β Fibril Formation. Journal of Structural Biology 130 (2), 259–270.
632 doi:10.1006/jsbi.2000.4289.

633 Merstorf, C., Cressiot, B., Pastoriza-Gallego, M., Oukhaled, A., Betton, J.-M., Auvray, L.,
634 Pelta, J., 2012. Wild type, mutant protein unfolding and phase transition detected by
635 single-nanopore recording. ACS chemical biology 7 (4), 652–658.
636 doi:10.1021/cb2004737.
637 Michaels, T.C.T., Šarić, A., Curk, S., Bernfur, K., Arosio, P., Meisl, G., Dear, A.J., Cohen,
638 S.I.A., Dobson, C.M., Vendruscolo, M., Linse, S., Knowles, T.P.J., 2020. Dynamics of
639 oligomer populations formed during the aggregation of Alzheimer's Aβ42 peptide. Nature
640 chemistry 12 (5), 445–451. doi:10.1038/s41557-020-0452-1.
641 Michaels, T.C.T., Šarić, A., Habchi, J., Chia, S., Meisl, G., Vendruscolo, M., Dobson, C.M.,
642 Knowles, T.P.J., 2018. Chemical Kinetics for Bridging Molecular Mechanisms and
643 Macroscopic Measurements of Amyloid Fibril Formation. Annual review of physical
644 chemistry 69, 273–298. doi:10.1146/annurev-physchem-050317-021322.
645 Nougadère, A., Sirot, V., Cravedi, J.-P., Vasseur, P., Feidt, C., Fussell, R.J., Hu, R., Leblanc,
646 J.-C., Jean, J., Rivière, G., Sarda, X., Merlo, M., Hulin, M., 2020. Dietary exposure to
647 pesticide residues and associated health risks in infants and young children - Results of the
648 French infant total diet study. Environment International 137, 105529.
649 Oukhaled, G., Mathé, J., Biance, A.-L., Bacri, L., Betton, J.-M., Lairez, D., Pelta, J., Auvray,
650 L., 2007. Unfolding of Proteins and Long Transient Conformations Detected by Single
651 Nanopore Recording. Phys. Rev. Lett. 98 (15), 158101.
652 doi:10.1103/PhysRevLett.98.158101.
653 Ouldali, H., Sarthak, K., Ensslen, T., Piguet, F., Manivet, P., Pelta, J., Behrends, J.C.,
654 Aksimentiev, A., Oukhaled, A., 2020. Electrical recognition of the twenty proteinogenic
655 amino acids using an aerolysin nanopore. Nat Biotechnol 38 (2), 176–181.
656 doi:10.1038/s41587-019-0345-2.

Phillips, J.C., Braun, R., Wang, W., Gumbart, J., Tajkhorshid, E., Villa, E., Chipot, C., Skeel, R.D., Kalé, L., Schulten, K., 2005. Scalable molecular dynamics with NAMD. Journal of computational chemistry 26 (16), 1781–1802. doi:10.1002/jcc.20289.

Piguet, F., Ouldali, H., Pastoriza-Gallego, M., Manivet, P., Pelta, J., Oukhaled, A. Identification of single amino acid differences in uniformly charged homopolymeric peptides with aerolysin nanopore. Nat Commun 9 (1), 1–13. doi:10.1038/s41467-018-03418-2.

Qiu, Y., Lin, C.-Y., Hinkle, P., Plett, T.S., Yang, C., Chacko, J.V., Digman, M.A., Yeh, L.-H., Hsu, J.-P., Siwy, Z.S., 2016. Highly Charged Particles Cause a Larger Current Blockage in Micropores Compared to Neutral Particles. ACS nano 10 (9), 8413–8422.

Rodriguez-Larrea, D., Bayley, H., 2013. Multistep protein unfolding during nanopore translocation. Nature Nanotech 8 (4), 288–295. doi:10.1038/nnano.2013.22.

Roman, J., Jarroux, N., Patriarche, G., Français, O., Pelta, J., Le Pioufle, B., Bacri, L., 2017. Functionalized Solid-State Nanopore Integrated in a Reusable Microfluidic Device for a Better Stability and Nanoparticle Detection. ACS applied materials & interfaces 9 (48), 41634–41640. doi:10.1021/acsami.7b14717.

Sánchez-Santed, F., Colomina, M.T., Herrero Hernández, E., 2016. Organophosphate pesticide exposure and neurodegeneration. Cortex 74, 417–426. doi:10.1016/j.cortex.2015.10.003.

Serra-Batiste, M., Ninot-Pedrosa, M., Bayoumi, M., Gairí, M., Maglia, G., Carulla, N., 2016. Aβ42 assembles into specific β-barrel pore-forming oligomers in membrane-mimicking environments. PNAS 113 (39), 10866–10871. doi:10.1073/pnas.1605104113.

Soto, C., Pritzkow, S., 2018. Protein misfolding, aggregation, and conformational strains in neurodegenerative diseases. Nature neuroscience 21 (10), 1332–1340. doi:10.1038/s41593-018-0235-9.

682 Stefureac, R., Waldner, L., Howard, P., Lee, J.S., 2008. Nanopore analysis of a small 86-
683 residue protein. Small (Weinheim an der Bergstrasse, Germany) 4 (1), 59–63.
684 doi:10.1002/smll.200700402.
685 Tavassoly, O., Lee, J.S., 2012. Methamphetamine binds to α-synuclein and causes a
686 conformational change which can be detected by nanopore analysis. FEBS letters 586
687 (19), 3222–3228. doi:10.1016/j.febslet.2012.06.040.
688 Waduge, P., Hu, R., Bandarkar, P., Yamazaki, H., Cressiot, B., Zhao, Q., Whitford, P.C.,
689 Wanunu, M., 2017. Nanopore-Based Measurements of Protein Size, Fluctuations, and
690 Conformational Changes. ACS nano 11 (6), 5706–5716. doi:10.1021/acsnano.7b01212.
691 Wälti, M.A., Ravotti, F., Arai, H., Glabe, C.G., Wall, J.S., Böckmann, A., Güntert, P., Meier,
692 B.H., Riek, R., 2016. Atomic-resolution structure of a disease-relevant Aβ(1-42) amyloid
693 fibril. PNAS 113 (34), E4976-84. doi:10.1073/pnas.1600749113.
694 Wang, H.-Y., Ying, Y.-L., Li, Y., Kraatz, H.-B., Long, Y.-T., 2011. Nanopore analysis of β-
695 amyloid peptide aggregation transition induced by small molecules. Analytical chemistry
696 83 (5), 1746–1752. doi:10.1021/ac1029874.
697 Yu, R.-J., Lu, S.-M., Xu, S.-W., Li, Y.-J., Xu, Q., Ying, Y.-L., Long, Y.-T., 2019. Single
698 molecule sensing of amyloid-β aggregation by confined glass nanopores. Chem. Sci. 10
699 (46), 10728–10732. doi:10.1039/C9SC03260F.
700 Yusko, E.C., Johnson, J.M., Majd, S., Prangkio, P., Rollings, R.C., Li, J., Yang, J., Mayer,
701 M., 2011. Controlling protein translocation through nanopores with bio-inspired fluid
702 walls. Nature Nanotech 6 (4), 253–260. doi:10.1038/nnano.2011.12.
703 Yusko, E.C., Prangkio, P., Sept, D., Rollings, R.C., Li, J., Mayer, M., 2012. Single-particle
704 characterization of Aβ oligomers in solution. ACS nano 6 (7), 5909–5919.
705 doi:10.1021/nn300542q.

706 Zhao, Y., Janot, J.-M., Balanzat, E., Balme, S., 2017. Mimicking pH-Gated Ionic Channels by
707 Polyelectrolyte Complex Confinement Inside a Single Nanopore. Langmuir : the ACS
708 journal of surfaces and colloids 33 (14), 3484–3490. doi:10.1021/acs.langmuir.7b00377.
709